

Detectors for the Linear Collider

Chapter 15 Detectors for the Linear Collider

1 Introduction

The linear collider detector must be optimized for physics performance, taking consideration of its special environment. To plan for this detector, we consider the physics requirements of the linear collider and build on the experience of operating SLD at the SLC.

The detector must be hermetic, with good charged-track momentum and impact parameter resolution. The calorimeter must provide good resolution, with good granularity, particularly in the electromagnetic section. Electron and muon identification must be done efficiently.

The beamline conditions of the linear collider motivate a strong solenoidal magnetic field to contain the vast number of low-energy electron-positron pairs. There must be provision for an accurate measurement of the differential luminosity, and for timing information that will be useful to separate interactions from separate bunches within a bunch train.

This chapter begins with a discussion of the major issues for the linear collider detector, starting from the beamline conditions and working through the subsystems. Following this discussion, three potential detectors developed for the NLC are described, two designed for the higher-energy IR, and the third for the second IR, where the lower-energy operation is foreseen. Other detectors have been considered in Europe [1] and Asia [2].

These detector studies have been undertaken to understand how well the diverse physics measurements at a linear collider can be accomplished, to provide preliminary guidance on costs, and to highlight areas where R&D is needed. The specific choices of technology and full detector optimization will await the formation of LC experimental collaborations.

2 Interaction region issues for the detector

2.1 Time structure.

The NLC is expected to operate with trains of 190 bunches with 1.4 ns bunch spacing. This time structure requires that the beams cross at an angle. It also affects the number of bunches seen within the integration time of any detector subcomponent and has a strong influence on the types of feedback schemes that can be used to keep the beams in collision.

Crossing angle and parasitic collisions. In order to avoid parasitic collisions, a crossing angle between the colliding beams is required. The minimum angle acceptable for this beam-beam limit is approximately 4 mrad for the NLC parameters. A larger angle is desirable because it permits a more straightforward extraction of the spent beams (see Fig. 15.1), but an excessively large crossing angle will result in a luminosity loss. The angle between the beams chosen in the NLC design is 20 mrad.

The bunches must interact head-to-head or there will be a substantial loss of luminosity. RF cavities that rotate each bunch transversely will be located 10–20 m on either side of the IP. At 20 mrad crossing angle, the relative phasing of the two RF pulses must be accurate to within 10 μm to limit the luminosity loss to less than 2%. This corresponds to 0.04 degrees of phase at S-band (2.8 GHz). The achievable resolution is about 0.02 degrees, which sets an upper limit on the crossing angle of 40 mrad.

Solenoid field effects. The crossing angle in the x - z plane causes the beam to see a transverse component of the detector's solenoid field. If uncorrected, this field will deflect the beams so they do not collide. Likewise, the deflection would cause dispersion that would blow up the beam spot size. Both of these effects can be cancelled by judiciously offsetting the position of the last quadrupole, QD0, and steering the beam appropriately. Synchrotron radiation emission in the transverse field leads to an irreducible increase in spot size. This effect is proportional to $(L^* B_S \theta_C)^{5/2}$, where L^* is the distance between the IP face of the last magnet and the interaction point. While it is small at the values of L^* , B_S , and θ_C considered to date, this effect might someday limit the design of the detector and IR.

After the beams collide at the IP, they are further bent by the solenoid field. Since compensating for this energy-dependent position and angle change with independent dipoles is difficult, the extraction line must be adjusted appropriately for the chosen beam energy. Realignment will be required if the extraction line does not have adequate dynamic aperture to accommodate the full range of beam energies used in experiments.

Finally, if the permeability of QD0 is not exactly unity, the field gradient of the solenoid in the detector endcap region will result in forces on QD0 that will need to be compensated. This may influence the schemes considered to compensate for nanometer-level vibration compensation of the magnet.

2.2 IR layout

Magnet technology. The NLC/JLC and TESLA designs have chosen to use different technologies for the final quadrupole doublet. The choices are dictated by the choice of crossing angle, and by the scheme to extract the spent beam after the collision. The NLC approach is to extract outside the outer radius of a compact Rare Earth Cobalt (REC) magnet into an extraction line that begins 6 m from the IP. The REC of choice is $\text{Sm}_2 \text{Co}_{17}$, because of its radiation-resistant properties. Since the

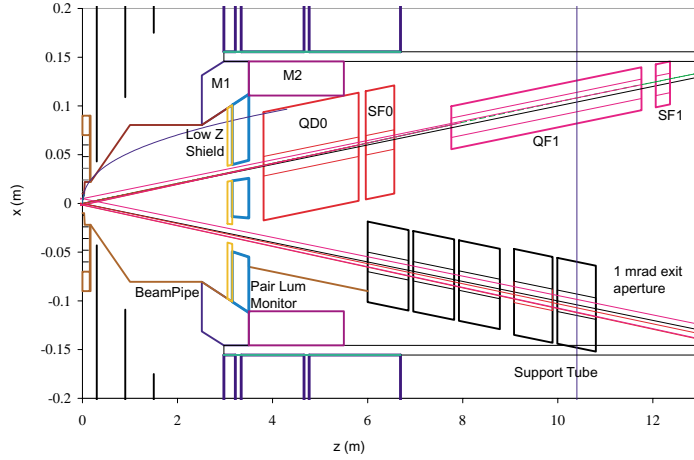


Figure 15.1: IR Layout for the NLC Large Detector.

final quadrupoles can be made light and stiff and have no external power connections, they are well suited for vibration stabilization. The downside to this choice is a lack of flexibility. Other issues that need to be explored further are the compatibility of the REC material with the solenoid field of the detector and the variation of the magnetic field with temperature.

In the current design $L^* = 3.8$ m. An additional 30 cm of free space has been left in front of the pair luminosity monitor to allow for different magnet configurations as the beam energy is increased. Increasing L^* provides more transverse space for the final quads and moves their mounting points further outside the detector, where they can presumably be better stabilized. By keeping L^* larger than the minimum z of the endcap calorimeter, the heavy W/Si-instrumented mask described below can be better incorporated into the detector's acceptance and mechanical structure. By increasing the distance between the IP and the first piece of high- Z material seen by the beam, one can minimize the effect of backscattered debris from the interaction of off-energy e^+e^- pairs created when the beams interact.

On the other hand, increasing L^* tightens the tolerances of the Final Focus optics and reduces its bandwidth. Synchrotron radiation produced by beam halo particles in the final lenses determines the minimum radius of the beam pipe inside the vertex detector. The larger L^* is, the larger will be the fan of photons shining on the vertex detector.

Masks. The electrons and positrons produced in pairs in the beam-beam interaction have a mean energy of about 13 GeV at $\sqrt{s} = 1$ TeV. These off-energy particles spiral in the detector's solenoid field and strike the pair-luminosity monitor or the inner bore of the extraction line magnet. The main purpose of the masking is to

shield the detector from the secondary particle debris produced when an e^\pm interacts. There are three masks foreseen. M1 begins at the back of the pair luminosity monitor and extends 0.64 m in z beyond its front face; its inner angle is set by the requirement that it stay just outside the so-called “dead cone” through which the pairs coming from the IP travel. With the mask tip at 2.5 m, a 3 T field requires an inner angle of 32 mrad. This mask would ideally be made of W/Si and be fully integrated with the detector’s calorimetry. M2 is a simple tungsten cylinder. The last mask near the IP is a 10–50 cm layer of low- Z material (*e.g.*, Be or C) that absorbs low energy charged particles and neutrons produced when the pairs hit the front face of the W/Si pair luminosity monitor. The very low-energy charged secondaries would otherwise flow back along the solenoid’s field lines toward the vertex detector (VXD) and produce unacceptable backgrounds.

2.3 Small spot size issues

The beams must be held stable with respect to one another in the vertical plane at the level of one nanometer. Measurements in existing detectors imply that the mounting of the final quadrupoles may have to correct as much as 50 nm of vibration, caused mostly by local vibration sources and to a much lesser extent by naturally occurring seismic ground motion. Concerns about vibrations caused by moving fluids lead to the choice of permanent magnets for QD0 and QF1. These magnets will be mounted in cam-driven mover assemblies and the beam-beam interaction used to control their position to compensate for disturbances at frequencies below about $f/20$, where f is the beam repetition rate of 120 Hz.

For frequencies above 5–6 Hz, the NLC strategy for stabilizing luminosity relies on a combination of passive compliance (minimizing and passively suppressing vibration sources while engineering to avoid resonant behavior) and active suppression techniques. Quad motion will be measured either optically relative to the surrounding bedrock or inertially, and a correction will be applied to either the final doublet position (via an independent set of magnet movers) or its field center (via a corrector coil). Finally, there will be feedback based on the measured beam-beam deflection. Such a system can respond sufficiently rapidly (within 15 ns) to correct the trailing bunches in a train, once the first few are used to measure any collision offset.

2.4 The beam-beam interaction

The two main experimental consequences of the beam-beam interaction are a broadening of the energy distribution, due to the emission of photons by one beam in the field of the oncoming beam, and the subsequent background generated by interactions of those photons. The beamstrahlung contribution to the energy spread must be considered together with the intrinsic energy spread of the accelerator and the effect of initial state radiation. These effects have been taken into account in the

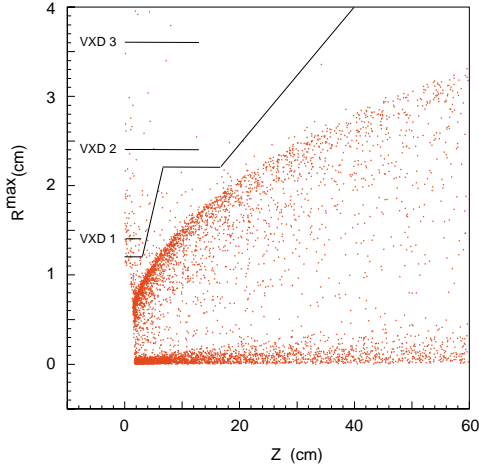


Figure 15.2: R_{\max} vs. z distribution of pairs in a 3 Tesla solenoid field. R_{\max} is the maximum radius the particle travels from the IP, plotted at the z corresponding to the first apex of its helical trajectory.

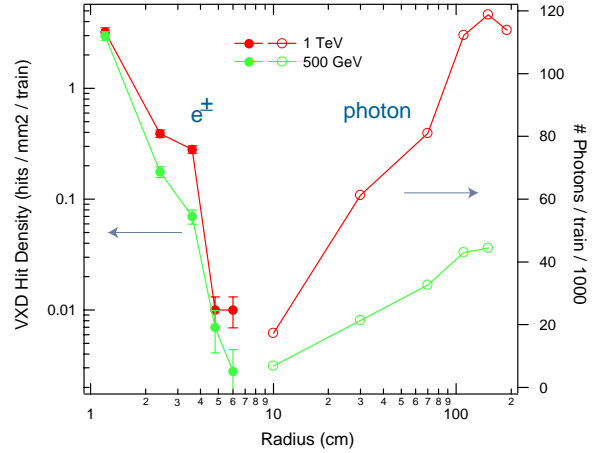


Figure 15.3: Charged particle hit density per train in the VXD, and the absolute number of photons per train entering the TPC within $|\cos\theta| < 0.92$, as function of radius.

discussion of the various physics process. Below we discuss the beam-beam interaction as a potential source of backgrounds.

e^+e^- pairs and the minimum solenoid field. The incoherent production of e^+e^- pairs arising from Bethe-Heitler ($e^\pm\gamma \rightarrow e^\pm e^+e^-$), Breit-Wheeler ($\gamma\gamma \rightarrow e^+e^-$), and Landau-Lifshitz ($e^+e^- \rightarrow e^+e^-e^+e^-$) processes is the main source of background at the present generation of planned linear colliders. At CM energies of 1 TeV, roughly 10^5 particles are produced each bunch crossing, with a mean energy of 13 GeV. Very few particles are produced at a large angle and the dominant deflection is due to the collective field of the oncoming beam. The so-called ‘dead cone’ that is filled by these particles is clear in the R_{\max} vs. z plot in Fig. 15.2. The beam pipe inside the VXD innermost layer must be large enough and short enough that it does not intersect this region.

Secondary particles and their sources. Secondary particle backgrounds—from neutrons, photons, and charged particles—can be a problem for the detector whenever primary particles or particles from the collision are lost close to the IP. The main purpose of the masking described earlier is to limit the backgrounds these secondaries produce. Figure 15.3 shows the charged particle hit density per train in the VXD as a function of radius, and the absolute number of photons per train entering the TPC within $|\cos\theta| < 0.92$. The most important sources of secondary particles are as follows:

- e^+e^- pairs striking the pair luminosity monitor are the most important source

of secondaries as the pairs are well off the nominal beam energy, spiral in the detector's field and strike high-Z materials close to the IP. Backgrounds from this process are controlled by the masks described above.

- Radiative Bhabhas are a source of off-energy particles that are outside the energy acceptance of the extraction line. However, they are sufficiently few in number and leave the beam line sufficiently far from the IP that they are not an important background for the main detector elements.
- The low-energy tail of the disrupted beam cannot be transported all the way to the dump. The current design of the extraction line includes a chicane to move the charged beam transversely relative to the neutral beam of beamstrahlung photons. The bends at the beginning and the end of the chicane are the primary locations where particles are lost. The number of particles lost, $\sim 0.25\%$ of the beam, and the separation of the loss point from the IP makes this an unimportant background source for the main detector, but calls into question the viability of sophisticated instrumentation, such as a polarimeter and an energy spectrometer, in the extraction line.
- Neutrons shining back on the detector from the dump are controlled by shielding immediately surrounding the dump, placing concrete plugs at the tunnel mouths, maximizing the distance from the dump to the IP, and minimizing window penetrations in the concrete. The detector of most concern is the VXD, which can look into the dump with an aperture equal to that provided to accommodate the outgoing beamstrahlung photons and synchrotron radiation.

Beamstrahlung photons. At 500 GeV, 5% of the beam power is transformed into beamstrahlung photons; this rises to 10% at 1 TeV. The IR is designed so that these photons pass unimpeded to a dump. This consideration, along with the angular spread of the synchrotron radiation (SR) photons, determines the exit aperture of the extraction line, currently set at 1 mrad. The maximum transverse size of the dump window that can be engineered and the beamstrahlung angular spread set the maximum distance the dump can be located from the IP. That distance and the size of the aperture in the concrete blockhouse surrounding the dump determine the level of neutron backshine at the detector.

Hadrons from $\gamma\gamma$ interactions. Beamstrahlung photon interactions will also produce hadrons. For the TESLA 500 GeV IP parameters it is estimated that there is a 2% probability per bunch crossing of producing a hadronic event with $p_{T\min} > 2.2$ GeV [3]. The average number of charged tracks is 17 per hadronic $\gamma\gamma$ event, with 100 GeV deposited in the calorimeter. This study needs to be repeated for the NLC IP parameters and detector acceptance. Nonetheless, we can estimate the severity of this background by scaling the rate from the TESLA study by the square of n_γ , the

average number of photons produced by beamstrahlung, giving a factor $((1.2/1.6)^2)$, and also taking the bunch structure (190/1) into account. This leads to an event probability of 2.2 events/train with 220 GeV in the calorimeter at $\sqrt{s} = 500$ GeV. It would clearly be advantageous to be able to time-stamp the hit calorimeter cells and tracks with the bunch number that produced them and thereby limit the background affecting a physics event of interest.

Muons and synchrotron radiation. SR photons arise from the beam halo in the final doublet, as shown in Fig. 15.4. The limiting apertures of the IR layout determine the maximum angular divergence of the charged particles that can be tolerated. Particles above the maximum divergence must be removed by the accelerator's collimation system. If the VXD radius is too small, the apertures in the collimation system required to remove the beam halo will be unreasonably small and will produce wakefields that will lead to beam spot size increases and a loss of luminosity. As particles are scraped off by the collimation system, muons are produced. Depending on the level of the halo and the robustness of the detector against background muons, a magnetic muon spoiler system may be required.

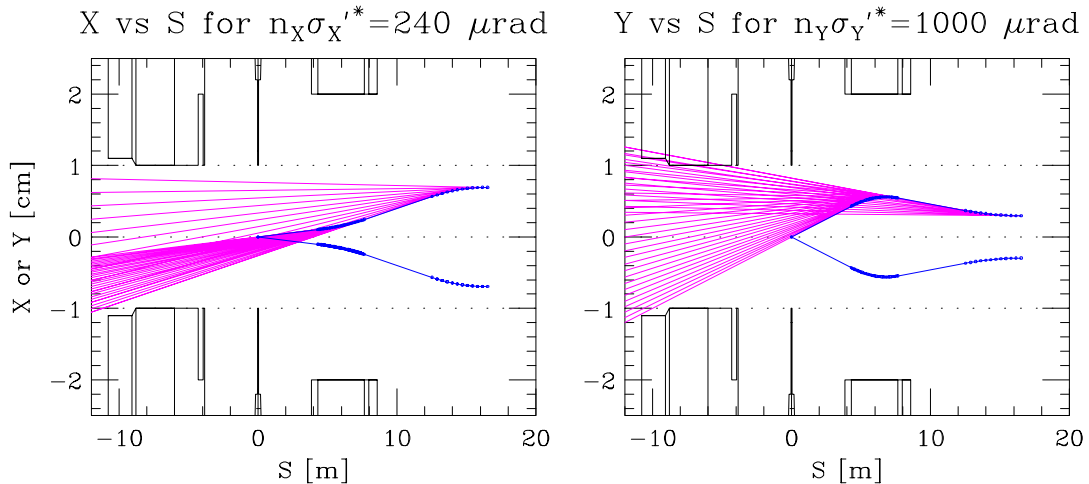


Figure 15.4: Synchrotron radiation fans from beam halo particles .

3 Subsystem considerations

3.1 Vertex detector

Recent experiments have benefited enormously from investments in excellent vertex detectors. An important lesson has been the immense value of a pixelated detector. This technology enabled SLD to match many of the physics measurements

at LEP with a much smaller data sample. The physics goals of the linear collider will also demand optimal vertex detection. The physics signals are rich in secondary vertices, and event rates are limited, demanding highly pure and efficient tagging.

Physics processes requiring vertex detection include the Higgs branching ratios, SUSY Higgs searches such as $A \rightarrow \tau^+ \tau^-$, searches for staus, top studies, improved measurement of W pairs, Z' studies such as τ polarization, and Z pole physics. Some processes will involve several heavy quark decays, complicating the reconstruction, and increasing the demand for pixelated detectors. The physics will require highly efficient and pure b and c tagging, including tertiary vertex reconstruction, and charge tagging (as needed for b/\bar{b} discrimination, for example). Optimal performance calls for point resolutions better than $4 \mu\text{m}$, ladder thickness under $0.2\% X_0$, inner layers within 2 or 3 cm of the interaction point, coverage at least over $|\cos\theta| < 0.9$, and good central tracking linked to the vertex detector. The accelerator time structure and radiation environment will constrain the design, and must be carefully considered.

A pixel CCD vertex detector was developed at the SLC. The SLD vertex detector, VXD3 [4], comprised 307 million pixels on 96 detectors, and achieved $3.8 \mu\text{m}$ point resolution throughout this large system. With such exceptional precision, extremely pure and efficient flavor tagging at the Z -pole was possible: 60% b tagging efficiency with >98% purity, and better than 20% c tagging efficiency with 60% purity. SLD also achieved exceptional charge separation between b and \bar{b} . The value of the pixel detector has been clearly established, even in the relatively clean environment of the SLC, where the hit occupancy in VXD3 was about 10^{-4} . These successes motivate the choice of CCDs for the next-generation linear collider, where even better performance is foreseen.

The main weaknesses of the CCD approach to vertex detection are the slow read-out speed and the radiation sensitivity. The speed issue can be managed at the linear collider, as SLD demonstrated. The hit density is maximal at the inner radius, where one expects about 3 per mm^2 per bunch train at 1.2 cm. This rate of $\sim 10^{-3}$ per pixel is challenging, but manageable, especially when the inner layer hits are matched to tracks reconstructed outside this layer.

With regard to the radiation background, the neutrons create the major challenge. Fluences greater than $10^9/\text{cm}^2/\text{year}$ are expected. CCDs are expected to withstand this level of radiation. However, since the neutron backgrounds could be larger, CCDs with engineered rad-hard enhancements are being studied [5].

Despite the established performance of the CCD vertex detector, active pixels do provide interesting alternatives. They can be inherently less sensitive to radiation damage (hence the interest in using them at the LHC), but generally have been less precise, and they contain more material leading to multiple scattering. Efforts are underway to close the gap between the demonstrated CCD performance and the state of the art in active pixels. These efforts will be followed closely.

Central tracking is vital to the performance of the vertex detector. With severely

limited momentum resolution of its own, the vertex detector relies on the momentum measurement of the tracker for inward projection of tracks.

3.2 Tracking

Tracking of high-energy isolated charged particles will be important at a linear e^+e^- collider. Isolated leptons are prevalent in many new physical processes, including production of sleptons, heavy leptons, and leptoquarks, and in many interesting Standard Model processes, notably in associated hZ production where the Z decays into charged leptons. While the calorimeter may provide a good measure of electron energy (but not electric charge), excellent tracking will be needed to measure high muon energies and the charged decay products of τ 's.

Reconstruction of hadron jets will also be important, both in searching for new physical processes and in understanding Standard Model channels. Compared to the high-energy leptons discussed above, charged hadrons in jets have much lower average energies, relaxing the asymptotic $\sigma(1/p_t)$ requirements. But tracking these hadrons well requires good two-track separation in both azimuth (ϕ) and polar angle (θ). Aggressive jet energy flow measurement also requires unambiguous extrapolation of tracks into the electromagnetic calorimeter, again demanding good two-track separation and also good absolute precision.

Forward-angle tracking is expected to be more important at a linear collider than has been traditionally the case for e^+e^- detectors. Some supersymmetry processes have strongly forward-peaked cross sections. Furthermore, in order to monitor beamstrahlung adequately, it is likely that precise differential luminosity measurement will be necessary, including accurate (0.1 mrad) polar angle determination of low-angle scattered electrons and positrons [6].

The central tracker cannot be considered in isolation. Its outer radius drives the overall detector size and cost. Given a desired momentum resolution the tracker's spatial resolution and sampling drive the required magnetic field. This affects the solenoid design, including the flux return volume.

For a detector with a compact silicon vertex detector and a large gas chamber for central tracking, an intermediate tracking layer can improve momentum resolution, provide timing information for bunch tagging, and serve as a trigger device for a linear collider with a long spill time.

The most important technical issue for the tracking system is designing to meet a desired resolution in $1/p_t$ of order 10^{-5} GeV^{-1} . This goal is driven by mass resolution on dileptons in Higgsstrahlung events and by end-point resolution in leptonic supersymmetry decays. There are tradeoffs among intrinsic spatial resolution, the number of sampling layers, the tracking volume size, and the magnetic field. The choices affect many other issues. For example, pattern recognition is more prone to ambiguities for a small number of sampling layers, with in-flight decays a particular problem. Matching to the vertex detector and achieving good two-track separation is more

difficult for large intrinsic spatial resolution. A large magnetic field distorts electron drift trajectories for several tracking technologies. High accelerator backgrounds may lead to space charge buildup in a time projection chamber (TPC), degrading field uniformity and hence resolution. More generally, though, high backgrounds tend to favor choosing a TPC or another device which makes 3-dimensional space point measurements (such as a silicon drift detector) over a device with 2-dimensional projective measurements (such as an axial drift chamber or silicon microstrips). On the other hand, a pixel-based vertex detector may provide adequate ‘seeds’ for tracks, even in the presence of large backgrounds.

Material in the tracker degrades momentum resolution for soft tracks and increases tracker occupancy from accelerator backgrounds due to Compton scattering and conversions. Because front-end electronics can be a significant source of material, readout configuration can be quite important, affecting detector segmentation and stereo-angle options. Achieving polar angle resolution comparable to the azimuthal angle resolution may be expensive and technically difficult.

As mentioned above, accelerator backgrounds can degrade track reconstruction via excessive channel occupancy. One possible way to ameliorate the effects of this background is via bunch tagging (or bunch-group tagging) of individual tracking hits, but such tagging may place strong demands on the tracker readout technology.

3.3 Calorimetry

3.3.1 Energy flow

The first question for calorimetry at the linear collider is one that not only influences the overall philosophy of this system but also has ramifications for other detector subsystems and for the overall cost: Should the calorimeter be optimized to use the ‘energy flow’ technique for jet reconstruction? The promise of substantial improvement in resolution using this technique is appealing. However, quantitative measures of this improvement are still being developed, and it is likely that an energy flow calorimeter will be relatively complicated and expensive because of the fine segmentation and high channel count.

Clearly, multi-jet final states will be important for LC physics. Examples from the physics program include separation of WW , ZZ , and Zh in hadronic final states, identification of Zhh , and $t\bar{t}h$ in hadronic decays, and full reconstruction of $t\bar{t}$ and WW events in studies of anomalous couplings and strongly-coupled EWSB. A further example comes at high energy from the processes $e^+e^- \rightarrow \nu\bar{\nu}WW$ and $e^+e^- \rightarrow \nu\bar{\nu}t\bar{t}$, where because of low statistics and backgrounds, one would need good jet-jet mass resolution without the benefit of a beam energy constraint. Indeed, one of the often-stated advantages of the e^+e^- environment is the possibility to reconstruct many types of final states accurately. In some instances, this is the key to the physics performance.

The energy flow (EF) technique makes use of the fact that the modest momenta of charged hadrons within jets are more precisely determined in the tracking detectors, than with a calorimeter. On the other hand, good energy resolution for photons (from π^0 decay) is achieved using any standard technique for electromagnetic calorimetry. Long-lived neutral hadrons (mostly K_L^0) are problematic using any technique, but they cannot be ignored. Therefore, a calorimeter designed to take advantage of EF must efficiently separate neutral from charged particle energy depositions. Such designs are characterized by a large tracking detector (radius R), a large central magnetic field (B), and an electromagnetic calorimeter highly segmented in 3-D. A figure of merit describing the ability to separate charged hadrons from photons within a jet is BR^2/R_m , where R_m is the Moliere radius of the electromagnetic calorimeter (EMCal). The EMCal's transverse segmentation should then be less than R_m in order to localize the photon showers accurately and distinguish them from charged particles. Similarly, the separation of the long-lived neutral hadrons from charged hadrons improves with BR^2 and a finely segmented hadron calorimeter (HCal). The reconstruction process involves pattern recognition to perform the neutral-charged separation in the calorimeter, followed by a substitution of the charged energy with the corresponding measurement from the tracker.

The advantage of EF is clear in principle. Whether the advantage is borne out with realistic simulation is not yet resolved, as the tools required to do justice to the technique are still under development. With their silicon/tungsten EMCal, the TESLA group currently finds [7] $40\%/\sqrt{E}$ for jet energy resolution (where E is the jet energy in GeV). They expect this to improve to $30\%/\sqrt{E}$ with progress in pattern recognition. Assuming that such good performance is indeed achievable with EF, it is useful to identify how this would improve the physics outlook, and at what cost.

3.3.2 Resolution, segmentation, and other requirements

There is no compelling argument from LC physics that demands outstanding photon energy resolution, resulting for example from an EMCal using high- Z crystals. Furthermore, such an optimization would not be consistent with the high degree of segmentation required for excellent jet reconstruction. Instead, the requirements for calorimetry from LC physics are jet energy and spatial resolution, and multi-jet invariant mass resolution. The required jet energy resolution depends, of course, on specific physics goals. A recent study [8] indicates that a resolution of $40\%/\sqrt{E}$ is necessary to measure the Higgs self-coupling using Zhh final states. One benchmark for jet-jet mass resolution is the separation of W and Z hadronic decays in WW , ZZ , and Zh events. Both of these requirements may be achievable using energy flow reconstruction.

Segmentation is a critical parameter, since an EF design requires efficient separation of charged hadrons and their showers from energy depositions due to neutrals.

The typical charged-neutral separation, Δx , is derived from the particle density in jets after they pass through the tracking detectors. This depends upon the physics process and \sqrt{s} , as well as the tracker radius and the detector magnetic field. Studies show that the minimum Δx is typically 1–4 cm in the EMCal and about 5–10 cm in the HCal. The EMCal should be very dense, with Moliere radius of a few cm or less, and should have transverse segmentation that is smaller still, in order to localize the photon showers accurately. Fine longitudinal segmentation, with each layer read out, is also essential in order to track the charged particles through the EMCal and to allow charged-neutral separation in 3-D. This will also benefit the energy resolution for photons and electrons. There is no reason to organize the layers in towers, and, in fact, this probably should be avoided. The fine transverse segmentation provides excellent electron identification and photon direction reconstruction. The latter is also useful for measuring photons which result from a secondary vertex. This is relevant, for example, in gauge-mediated SUSY, which can lead to secondary vertices with a photon as the only visible decay particle.

For EF in the HCal, it is desirable to track MIPs throughout. One would need to identify shower positions with a resolution of a few cm. Because of the relatively diffuse distribution of deposited energy for hadron-initiated showers, the solution for charged/neutral identification is not as obvious as for the EMCal case, and different ideas are under consideration. In any scheme, one requires a high degree of segmentation. This might be implemented, for example, using scintillator tiles roughly 5–10 cm on a side. Another idea is to push to finer segmentation, using, for example resistive plate chambers (RPCs), but without providing pulse height in the readout. Such a ‘digital’ hadron calorimeter is one of the options being considered for TESLA. This provides increased resolution for pattern recognition, but perhaps with poorer neutral hadron energy resolution.

As with this segmentation issue, many of the other properties of the HCal in an EF calorimeter remain uncertain. One example is the necessary total calorimeter depth in interaction lengths. Another is the placement of the solenoid coil. Since the fields are typically large, and the coils are at large radius, their thickness is not negligible. Qualitatively, for good performance one would prefer to have the coil outside the HCal. But the tradeoffs are not yet well understood quantitatively.

The EF jet resolution is dominated by the tracker momentum resolution, the calorimeter pattern recognition efficiency, and by the purity of charged/neutral identification. Hence, single-particle resolutions are less important. However, the current EF designs yield energy resolution A/\sqrt{E} in the range $A = 12\text{--}20\%$ for photons, and in the range $A = 40\text{--}50\%$ for single hadrons.

For a detector not designed to use energy flow, there are, of course, many traditional choices available. Assuming that jets are to be reconstructed using the calorimeter only, one might choose a compensating, sampling calorimeter with a tower geometry. One or more layers of detector with finer segmentation may be required

at the front of the EMCal, or at shower maximum, to aid with electron and photon identification. Such a calorimeter would certainly be cheaper than an EF device at a similar radius. At low \sqrt{s} , especially at the Z , this may suffice.

One also needs to consider Bhabha scattering in the calorimeter design. First, the final state e^\pm at $\sqrt{s}/2$ determines the upper end of the dynamic range of the EMCal readout. For example, for a dense EMCal, the ratio of deposited energy for Bhabha electrons to MIPs can be 10^3 to 10^4 , depending on segmentation. Secondly, the Bhabhas are used for luminosity measurements of two types. First, the Bhabha rate can be used to measure the absolute luminosity. Since this rate at intermediate to large angles (endcap and barrel) will be large compared to (known) physics processes, it would not be necessary to rely on a small-angle luminosity monitor (LUM), although a LUM would still be useful for crosschecks and operations. Running at the Z is an exceptional case where a precise LUM would be required. The Bhabhas also provide probably the best measurement of the luminosity spectrum, $d\mathcal{L}/dE$, because the Bhabha acolinearity is closely related to the beam energy loss. This is ideally measured at intermediate angles, and the EMCal endcap will need to be able to aid the tracker with this measurement.

In addition to Bhabha scattering, two other types of measurement have been discussed for the small-angle region. One is a measurement of the flux of pairs produced in the collision beam-beam interactions. This would provide immediate feedback to operators of a quantity closely related to the instantaneous luminosity. The other is small-angle tagging of the forward-scattered electron or positron resulting from a two-photon interaction. This is useful both in the study of the two-photon process itself and in reducing background in the study of processes such as slepton pair production which resemble two-photon reactions. Such a device would need to tag a single high-energy electron within the angular region flooded by low-energy pairs from the beam-beam interaction.

Finally, the small-angle elements of any calorimeter design must reflect the requirement to limit the detector contribution to the missing transverse momentum resolution. This contribution is roughly $E_b\theta_{\min}$, where E_b is the beam energy. Given the limited angular coverage of the central tracking systems, one should consider carefully what type of calorimetry should be used near θ_{\min} .

3.3.3 Technology options

For the dense, finely segmented electromagnetic calorimeter required for energy flow, layers composed of a tungsten radiator with silicon detectors (Si/W) are a natural choice. The Moliere radius of tungsten is small (9 mm), and the silicon is thin and easily segmented transversely. Si/W EMCal's are currently incorporated in two LC detector designs, the TESLA detector and the NLC SD detector described in Section 4.2. This option has one outstanding drawback, the cost of the silicon detectors.

Both TESLA and SD assume that a cost of roughly $\$3/\text{cm}^2$ can be achieved in the future with a very large order. This is about a factor two cheaper than current costs. There are a number of cost and performance optimization possibilities. For example, one would probably not need to sample the EMCal uniformly in depth, reducing the sampling frequency after about $12 X_0$. One could also improve the photon energy resolution by sampling with thicker silicon, at some small loss of Moliere radius.

Perhaps it is possible to design a competitive energy flow electromagnetic calorimeter at lower cost using an alternative to silicon, for example, scintillator tiles. The transverse segmentation is limited using present techniques by the inability to couple sufficient light to a readout fiber. Perhaps this can be improved. However, given the larger cells, sufficiently large B and R may compensate for the segmentation disadvantage. This is the rationale for the NLC L design described in Section 4.1. Another alternative being considered for TESLA is a Shashlik EMCal. Beam test results [9], using fibers of two lifetimes in order to achieve some longitudinal segmentation, have been impressive, but it is unclear whether the segmentation is sufficient for EF.

The hadron calorimeter for an EF detector is not as highly constrained as the EMCal. Here, scintillator tiles can be of size similar to present applications, say 8–10 cm on a side, with coupling to an optical fiber. Such a scheme is under consideration for the TESLA and NLC L and P designs. (The last of these is described in Section 4.3.) Other possibilities include the ‘digital’ option mentioned above, which might use, for example, double-gap RPC readout layers or extruded scintillator. The spatial resolution per layer might be about 1 cm.

If it were possible to relax the need for precise jet reconstruction, then one might forego EF, and save some money with a more traditional calorimeter. For example, the NLC P design uses modestly segmented towers built up from Pb/scintillator layers. This might also be implemented using liquid argon.

3.4 Muon detection

The main purpose of the LC muon system is to identify muons and provide a software muon trigger. A secondary purpose is to use the muon detector as backup calorimetry for those particles that penetrate beyond the normal hadron calorimeter. The signature for muons is their penetration through the calorimetry and the instrumented iron flux-return for the solenoid field.

The momentum of muons is determined from the central and forward tracking systems. This requires the association of tracks found in the instrumented flux-return with hits/tracks in the central and forward tracking detectors. Two conditions permit this: a reasonable density of hits in the inner layers of the tracking detectors and limited confusion from multiple scattering due to the electromagnetic and hadronic calorimeters between the inner tracking detectors and the front face of the muon detectors. These conditions are satisfied, since the maximum density of tracks, at a radius of 3 m, is about $1/\text{cm}^2$ [10] and the r - ϕ rms multiple scattering of a 10 GeV/c

muon is approximately 2 cm. The number of radiation lengths X_0 of material in front of the muon system for the three candidate detectors L, SD and P are 200, 88 and 125, respectively.

Muons are identified by their ionization in tracking chamber panels [10] or scintillator strips [11] in 2 cm gaps between 5 or 10 cm thick Fe plates that make up the barrel and end sections of the Fe return yoke for the central solenoidal magnetic field. RPCs are taken as the example technology. These planar devices can be built with appropriate perimeter shapes, and they do not contain wires that could break. Tracking hits from the avalanche produced in the RPC gaps are read out with strip electrodes that run in the ϕ and z directions. The spatial resolution of these strips is 1 cm per detector plane.

For the case of the L detector, it can be seen in Fig. 15.5 that the number of hits as a function of momentum for W pair production, plateaus at about 5 GeV with 25 instrumented gaps. The plot shows that in the 3 T field there will be very good efficiency if 15 or more hits are required in the muon tracking algorithm.

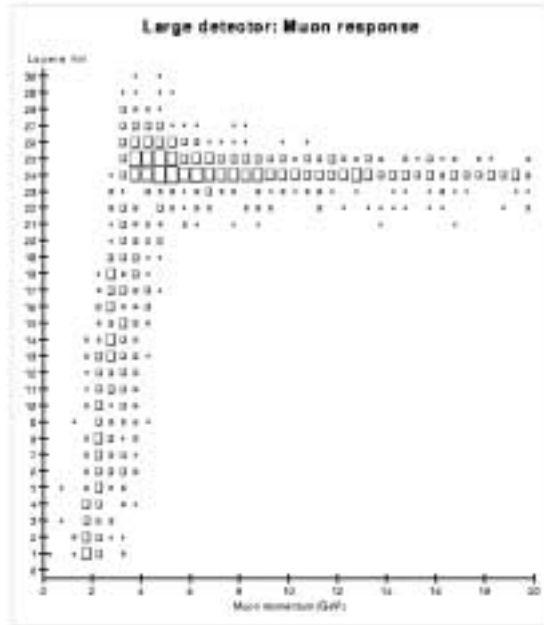


Figure 15.5: Hits in the muon system as a function of momentum for the L detector. The plot shows 10000 $e^+e^- \rightarrow W^+W^-$ events in which one W decays to a muon.

The Fe plate and strip readout for the muon system can be used as additional

coarse hadron calorimetry, since the number of interaction lengths λ for the L, SD and P options are, respectively, 6.6, 6.1 and 3.9. The muon Fe adds 7, 6, and 6 λ that can be used in the determination of residual hadronic energy with a resolution that will be about $1/\sqrt{E}$.

3.5 Solenoid

The detector is assumed to be a classical solenoidal design. The field in the tracking region ranges from 3 to 5 T for the various designs. The solenoid is assumed to be of the CMS type, based on a relatively thick, multi-layer superconducting coil. The radial thickness of the complete assembly is about 85 cm. The CMS vacuum shell has a total thickness of 12 cm, and a cold mass thickness of 31 cm (aluminum). It is likely that the cold mass thickness will scale roughly as B^2R . Then, the coil of the SD detector would be about 35% thicker.

The iron serves as the flux return, the absorber for the muon tracker, and the support structure for the detector. The (perhaps debatable) requirement of returning most of the flux drives the scale of the detector. At this stage of preliminary design, it is assumed that the steel is in laminations of 5 cm with 1.5 cm gaps.

The door structure very likely runs along the beamline past L^* , the position of the downstream face of the last machine quadrupole. Thus it is essentially certain that the Final Doublet (FD) is inside the detector, and quite possibly within the Hadronic Calorimeter. For this reason, the FD cannot be mounted on a massive column going directly to bedrock.

3.6 Particle ID

The physics topics of the linear collider do not demand hadron ID in a direct way, though the information may prove valuable for some analyses. Pions, kaons and protons are produced in the ratio of about 8:1:0.6 in high-energy e^+e^- colliders. The momentum spectrum of kaons in $q\bar{q}$ events at $\sqrt{s}=500$ GeV extends up to 150-200 GeV/c, posing a possibly unsurmountable ID measurement challenge. However, the average kaon momentum is only 10–17 GeV/c, and more than half of all kaons have momenta below 7 GeV/c. In t -quark and multi- b jet Higgs events, the multiplicity is higher, and so kaons have a slightly lower mean momentum.

The measurement of particle species distributions provides information on QCD processes and permits model tests, but the most important use of hadron ID may be to assist the application of other techniques, such as B tagging. As an example, two studies [12,13] have discussed the use of net kaon charge to tag the flavor of neutral B mesons produced in $q\bar{q}$ events. They find that with perfect knowledge of decay product identities in vertex-tagged neutral B mesons, roughly a quarter are correctly tagged by the net charge of kaons. The efficiency is much lower if all indiscriminated hadrons are used. It is a detailed, and so far unanswered, question whether the use of

hadron ID with realistic detector efficiencies can be an important tool to unscramble complex events that contain multiple b - or c -quark jets.

The geometric and, ultimately, the cost constraints limit the choice of technology for a hadron ID system of a linear collider detector. Ideally, it should take up no space and introduce no additional mass in front of the calorimeter. Traditional ionization measurement (dE/dx) in gas-based tracking chambers comes close to meeting these criteria.

The Time Projection Chamber (TPC) technology that appears in the TESLA and L tracker designs may be an optimal choice for combined tracking and ionization measurements for particle ID. The energy resolution that has been achieved with existing non-pressurized TPCs (*e.g.*, ALEPH at LEP) is 4.5%, which would yield π/K separation of better than 2σ for $p < 0.8$ GeV/c and 2-3 σ for $1.7 < p < 65$ GeV/c. One can improve the capability of a TPC by using pressurized gas to achieve 2.5% resolution, as demonstrated by the TPC at PEP. According to a recent model [14], this could provide 4σ π/K separation in the range $1.75 < p < 30$ GeV/c.

In practice, experiments that desire a high degree of species separation have supplemented ionization measurements with specialized devices such as time-of-flight, threshold Cerenkov or ring-imaging Cerenkov devices. The major drawback of a specialized hadron ID subsystem is its collateral impact on the tracking and calorimetry. All supplementary techniques take up radial space between the tracker and calorimeter, which means either shorter tracking volume or increased calorimeter radius with consequent cost and performance implications. Without a clearly defined need for the capability, it is difficult to justify a significant impact on the rest of the detector. For example, in the B^0 tagging study, even though the best performance was provided by an SLD-style CRID or a high-pressure TPC, relatively inexpensive improvements to an ALEPH-type TPC could achieve a sensitivity within a factor of two of these more complicated options but with little impact on the calorimetry.

In summary, at this stage there is no compelling argument to include a specialized hadron ID system in the high energy detector design, though in the process of optimizing the design this assumption may be reexamined.

3.7 Electronics and data acquisition

The NLC beam consists of 190 bunches spaced 1.4 ns apart, in trains that repeat at 120 Hz. There are variations with a doubled bunch spacing and an increased train frequency of 180 Hz, but these variations do not affect the basic theme. For most of the detector subsystems it will neither be possible, nor particularly desirable, to resolve bunches in a train. The train repetition rate of 120 Hz is a low frequency compared with Level 1 or Level 2 trigger rates at many other machines. There is no need for a hardware trigger, and (zero-suppressed, calibration-corrected) data can flow from the detector at this rate. A traditional Level 3 Trigger (software on a small set of processors) can select events for storage.

The time horizon for a detector is roughly 8 to 10 years away, which is at least 5 Moore's Law generations. To be sure, Moore's Law refers to computing power per dollar, but there are clearly related trends in most areas of silicon technology. At this time it seems most appropriate to sketch plausible architectures to help generate cost estimates, and to avoid detailed designs.

Perhaps the clearest distinction that should be made is the role of interconnections that are not on silicon. Rather inexpensive systems have been developed for large CCD detectors. The costs strongly reflect the number of output nodes that must be serviced, and correspond only weakly to the number of pixels being transmitted through that node. In addition, because of the train spacing, there is no penalty to serial multiplexing of the data from very large numbers of pixels. This is in contrast to the LHC, where there are many interactions associated with each beam crossing, which occurs every 25 ns. This is not to say there are no limits to the serial multiplexing. The readout of the SLD Vertex Detector crossed about 8 beam crossings at SLC, and it would be desirable to avoid this at the next-generation linear collider.

Consequently, we have developed the concept of clusters rather than channels. A cluster is a set of detector elements that can conveniently be processed and serialized into a single data stream, presumably an optical fiber. In the CCD example, each node might correspond to a cluster, although it might even be possible to handle multiple nodes in a single cluster. For the CCD case, we think of an ASIC located millimeters from the CCD and bonded to the CCD. This ASIC might handle the clock generation and the gate drives as well as the amplification and digitization of the CCD data. For silicon strip detectors, we foresee a single chip servicing a cluster of strips, presumably a complete detector a few cm wide. For a calorimeter utilizing scintillator and Hybrid Photo Diodes or Multi-Anode Phototubes, a cluster would correspond to all the outputs from each such device. In all cases, we avoid, as much as possible, all low-level cables and interconnects. The cluster reflects the mechanical nature of the detector. Some cases are less obvious. For a tungsten-silicon calorimeter, a cluster might correspond to a large area board carrying many close packed wafers of silicon diodes. It may cover perhaps a square meter or so. Variations on this concept would cover readout sectors of the TPC and the muon tracking detectors.

Thus the detector proper carries all the front end processing, and a relatively modest set of fibers carries data off the detector. We envision the fibers delivering the data to processors, perhaps based on VME, although there are hints that crate systems based on optical serial backplanes may arrive in time. These processor arrays would complete the signal processing, build the events, and pass those events to the system responsible for the Level 3 decision.

4 Detectors

Three detector models are now being studied as potential detectors for the NLC. These include two options for the high-energy IR, called L and SD, and one for the lower-energy, second IR, called P. Here we describe each of these detectors, and present some of their performance curves.

4.1 L detector for the high-energy IR

The L detector design is driven by the desire to provide a large tracking volume, to optimize tracking precision. This leads to a large-radius calorimeter and limits the magnetic field strength to about 3 Tesla.

The L detector is illustrated in Fig. 15.6. Table 15.1 presents the dimensions of the L detector, along with those for the SD and P detectors, described below.

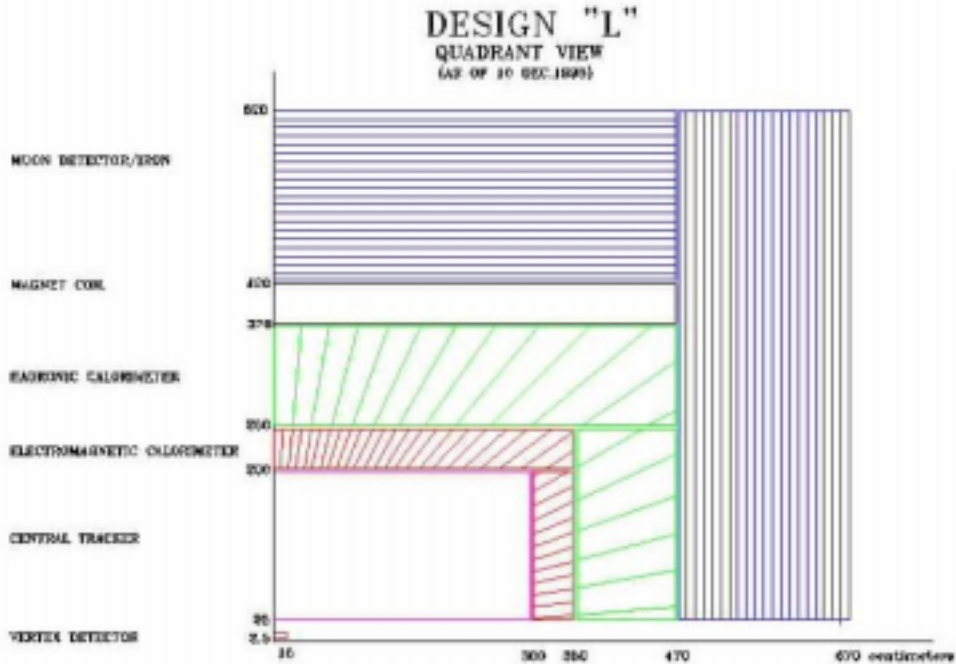


Figure 15.6: Quadrant view of the L detector.

The vertex detector is a five-barrel CCD vertex detector, based on the technology developed for SLD. The beam pipe radius of 1 cm allows the inner barrel of the detector to reside 1.2 cm from the IP. The inner barrel extends over 5 cm longitudinally. The other barrels have radii of 2.4 cm, 3.6 cm, 4.8 cm, and 6.0 cm, and they each extend 25 cm longitudinally. The barrel thicknesses are 0.12% X_0 and the precision

Component	L Detector				SD Detector				P Detector			
	R(cm)		Z(cm)		R(cm)		Z(cm)		R(cm)		Z(cm)	
	Min	Max	Min	Max	Min	Max	Min	Max	Min	Max	Min	Max
Vertex Det.	1.0	10	0	15	1.0	10	0	15	1.0	10	0	15
C.Track.	25	200	0	300	20	125	0	125	25	150	0	200
ECal												
Barrel	200	250	0	350	127	142	0	187	150	185	0	235
EndCap	25	200	300	350	20	125	172	187	25	150	205	240
HCal												
Barrel	250	370	0	470	143	245	0	289	215	295	0	320
EndCap	25	250	350	470	20	125	172	187	25	175	240	320
Magnet	370	420	0	470	248	308	0	289	185	215	0	235
Iron/Muon												
Barrel	420	620	0	470	311	604	0	290	295	425	0	320
EndCap	25	620	470	670	20	604	290	583	25	425	320	450

Table 15.1: Dimensions of the L, SD, and P Linear Collider Detectors.

is assumed to be $5 \mu\text{m}$. (This is taken as a conservative assumption, since SLD has achieved $3.8 \mu\text{m}$.) The entire system comprises 670,000,000 pixels of $20 \times 20 \times 20 \mu\text{m}^3$.

Figure 15.7 illustrates this system. The detector operates in an ambient temperature of 190°K , created by boil-off nitrogen. It is enclosed within a low mass foam cryostat. The same five-barrel CCD design has been assumed for the SD and P detectors below.

The performance of the vertex detector is illustrated in Figs. 15.8 and 15.9, where it is also compared to the SD and P Detector performance. The impact parameter resolution shown in Fig. 15.8 is shown to surpass the performance of SLD's VXD3. The bottom and charm tagging performance, shown in Fig. 15.9, is also seen to be exceptional.

The L detector central and forward trackers consist of a large-volume TPC, an intermediate silicon tracking layer (silicon drift detector or double-sided silicon microstrips), and five layers of double-sided, silicon microstrip disks in the forward regions. An additional scintillating-fiber intermediate tracker option has also been proposed to provide precise bunch timing. Figure 15.10 shows a sketch of the L detector tracking system.

A large-volume TPC with three-dimensional space point measurements along charged particle trajectories provides excellent pattern recognition (including recognition of long-lived particles that decay in the tracking volume) and good particle identification via dE/dx measurements. The baseline L detector TPC [15] has 144 tracking layers enclosed in a cylindrical volume of inner and outer radii = 50 and 200 cm, respectively, and of half-length 290 cm. The assumed resolutions on each hit are $150 \mu\text{m}$ in $r-\phi$ and 0.5 mm in $r-z$. A GEM-based readout has the potential to reduce

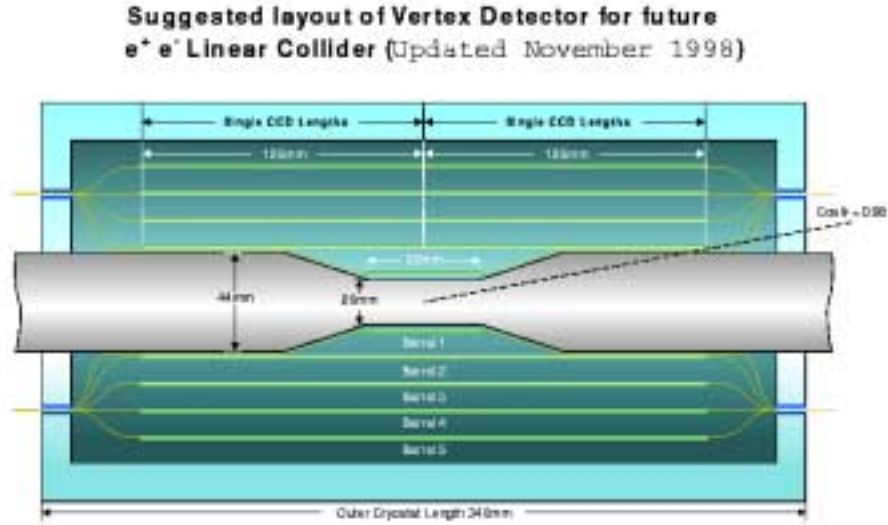


Figure 15.7: The five-barrel CCD vertex detector proposed for the linear collider.

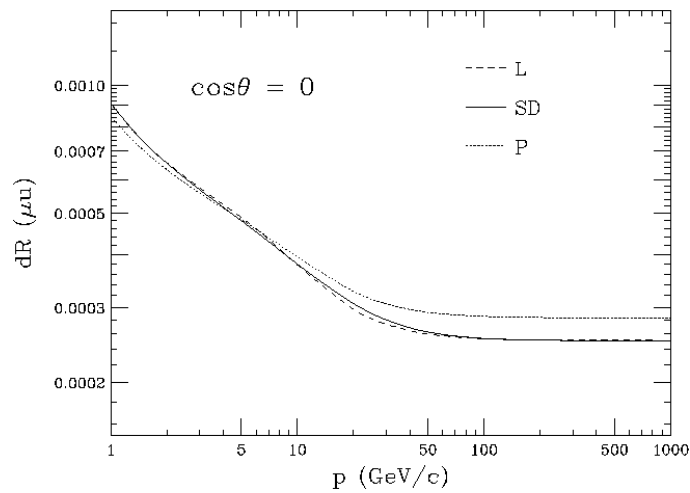


Figure 15.8: Impact parameter resolution versus momentum for the vertex detector shown in Fig. 15.7.

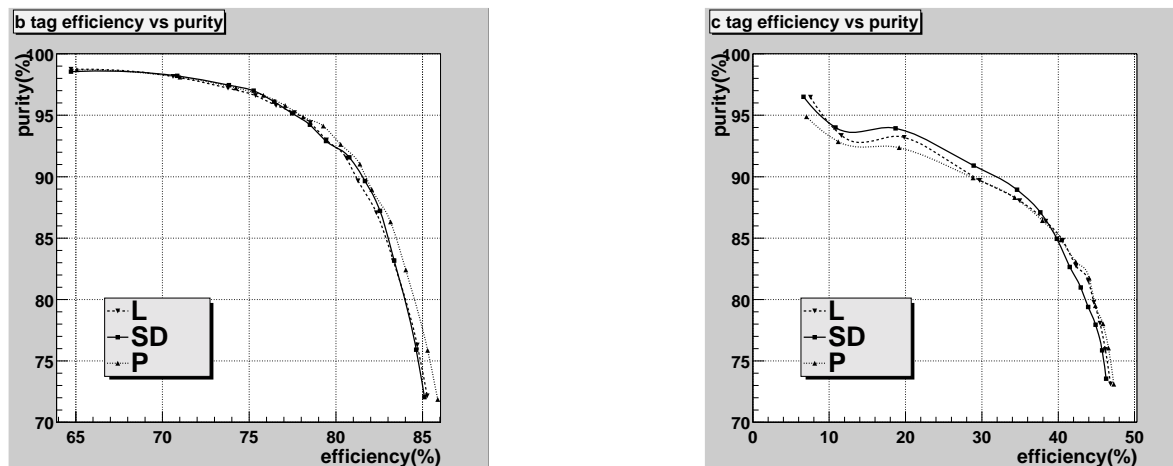


Figure 15.9: Vertex-tagging purity versus efficiency for b (left) and c (right), evaluated for decays of the Z^0 at $E_{\text{CM}} = 91.26$ GeV.

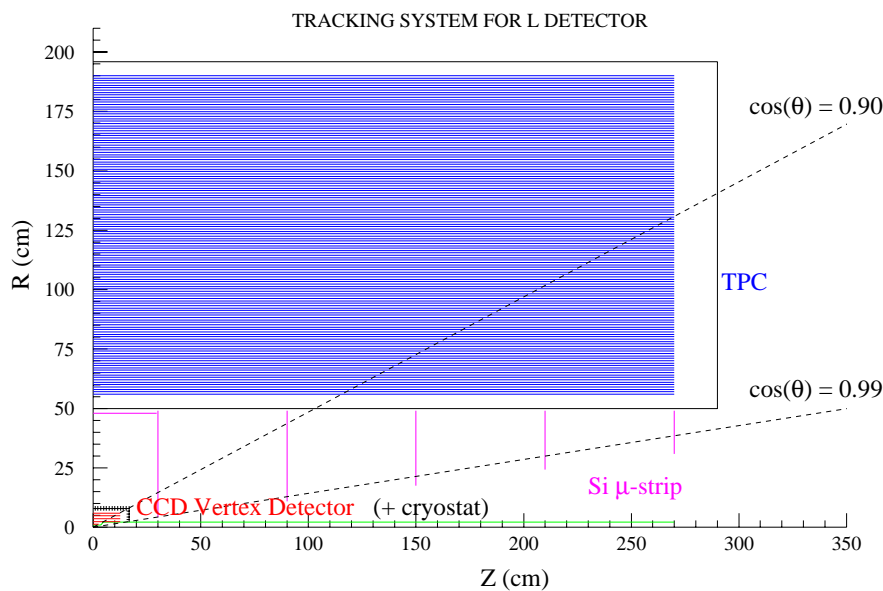


Figure 15.10: Sketch of L detector tracking system.

the r - ϕ resolution to $100 \mu\text{m}$. The small transverse diffusion for TPC operation in the 3 T magnetic field requires very narrow cathode pads and large total channel counts. Longer pads or the use of induced signal on adjacent pads may be considered to reduce the channel count. Good track timing resolution is obtained by requiring individual charged tracks to point back to a reconstructed vertex in the r - z plane. This timing resolution helps in reducing accelerator backgrounds.

The TPC in the STAR detector at RHIC has over 138,000 electronics channels and includes several design innovations. To reduce the required cable plant, low-noise low-power front end electronics are mounted on the TPC end planes. The analog signals are amplified, sampled and digitized before being sent to the DAQ system over fiber optics. A similar scheme is assumed here, with 20-MHz sampling, a 200-ns peaking time and 9-bit digitization.

The TPC analog front end electronics would consist of a high-bandwidth preamplifier and shaper amplifier (8-16 channels/ASIC chip), providing a 200 nsec peaking time pulse to the analog sampling and digitization section. The analog signals from the preamplifier and shaper amplifier would be sampled and stored with a high-frequency 20-MHz clock as they come in, and then digitized on a longer (10 μ sec) time scale as new samples are being taken. The recognition of charge cluster signals on a central cathode-pad channel triggers a switched capacitor array (SCA) to sample the channel and its nearest neighbors.

Gas mixtures of argon with methane and carbon dioxide are being considered, with Ar(90%):CH₄(5%):CO₂(5%) being quite attractive in balancing safety concerns, neutron-background quenching, and drift velocity. Positive ions feeding back from endplane gas amplification can be mitigated by the installation of a gating grid.

A silicon intermediate tracking detector just inside the TPC inner radius provides nearly a factor of two improvement in momentum resolution for high- p_t tracks and offers a pattern recognition bridge between the TPC and the vertex detector. Two silicon options are under consideration: a silicon drift detector and a double-sided silicon microstrip layer. In each case the layer would have a half-length of 29.5 cm and an average radius of 48 cm. The estimated space-point resolutions in r - ϕ and r - z are 7 μ m and 10 μ m, respectively, for the silicon drift detector option, with both at 7 μ m for the double-sided microstrip option.

An additional or alternative intermediate tracker constructed from scintillating fibers offers high-precision timing to allow the matching of tracks to individual beam bunches. The current NLC accelerator design provides beams composed of trains of bunches with bunch spacings of 1.4 ns. Large rates of two-photon interactions are expected both from interactions of virtual photons and from real photons created by beamstrahlung. The overlap of the two-photon events with e^+e^- annihilation events results in additional ‘mini-jets’, which can be a problem if tracks created in different bunch crossings are not separated. A scintillating-fiber intermediate tracker, coupled by clear fiber to visible light photon counters and read out by the SVXIIe chip [16] can achieve time resolutions on the order of 1 ns to associate tracks with individual bunches, as well as to complement time measurements in the TPC. Appropriate Si:As devices manufactured by Boeing [17] have a fast response time of less than 100 ps. One possible system consists of two axial layers and two 3°-stereo layers with a half-length of 29.5 cm at an average radius of 48 cm, supported by a carbon fiber cylinder. Scintillating fibers of diameter 800 μ m would provide individual measurements to

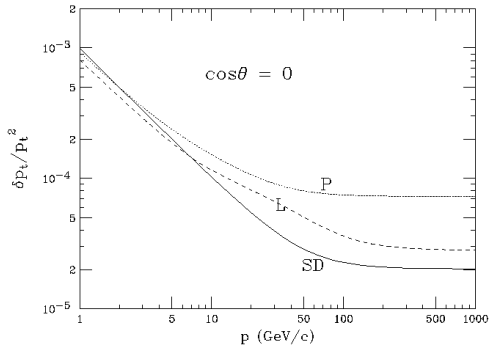


Figure 15.11: Expected fractional momentum resolution *vs.* momentum for the L, SD, and P central trackers for tracks transverse to the beam direction.

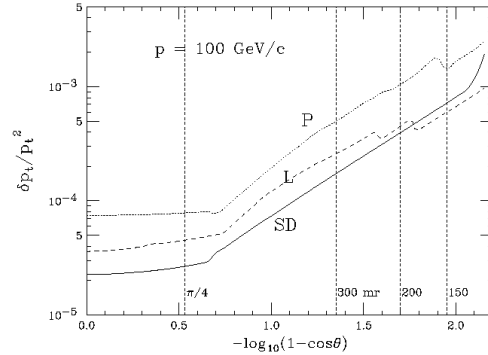


Figure 15.12: Expected fractional momentum resolution *vs.* $\cos\theta$ for the L, SD, and P central trackers for 100 GeV tracks.

230 μm and a combined point measurement with a precision of $\sim 100 \mu\text{m}$, resulting in a system with 15,000 channels.

As currently envisioned, the five layers of the L detector forward disk system are double-sided silicon microstrips, at distances of 30 cm to 270 cm from the interaction point, with fixed outer radii at 48 cm. Each side provides counterposing $\pm 20 \text{ mrad}$ r - ϕ stereo information, with a point resolution of 7 μm . For high-momentum tracks at $\theta = 300 \text{ mrad}$ ($|\cos\theta| = 0.955$), this small-angle stereo geometry provides a resolution in θ of about $\pm 300 \mu\text{rad}$. If large-angle (90°) stereo were used instead, the θ resolution would improve to about $\pm 100 \mu\text{rad}$. Although the layout of silicon strip detectors is more naturally suited to small-angle stereo, the demands placed on the θ resolution by the determination of the differential luminosity spectrum may force the consideration of large-angle stereo.

The performance of the L detector tracking system, including the CCD vertex detector, is summarized in Fig. 15.11, which shows fractional momentum resolution *vs.* momentum for tracks transverse to the beam direction ($\cos\theta=0$). Figure 15.12 shows the fractional momentum resolution *vs.* $\cos\theta$ for tracks of momentum 100 GeV. In the limit of high-momentum tracks, the L tracking resolution in $1/p_t$ is $3 \times 10^{-5} \text{ GeV}^{-1}$. Figure 15.13 shows the expected distribution in recoil mass from dimuons in the Higgsstrahlung process $e^+e^- \rightarrow hZ \rightarrow X\mu^+\mu^-$ at $\sqrt{s} = 350 \text{ GeV}$ for the nominal L detector baseline and for several globally rescaled resolutions in $1/p_t$.

The electromagnetic calorimeter of the L Detector is a lead-scintillator laminate with 4 mm lead followed by 1 mm scintillator for 40 layers. This results in 28.6 radiation lengths with a 2.1 cm Moliere radius. One layer of 1 cm^2 silicon pads is foreseen near shower maximum. The transverse segmentation of the scintillator is 5.2 cm \times 5.2 cm. The barrel of the electromagnetic calorimeter has an inner radius

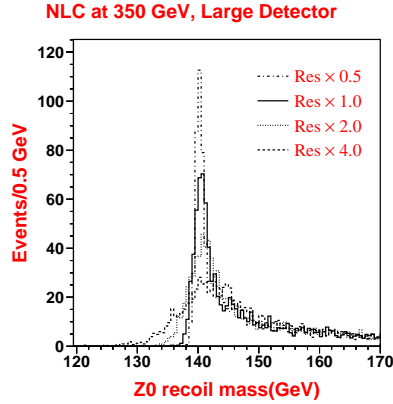


Figure 15.13: Expected recoil mass distribution in recoil mass from dimuons in the Higgsstrahlung process $e^+e^- \rightarrow hZ \rightarrow X\mu^+\mu^-$ at $E_{cm} = 350$ GeV for the nominal L detector baseline and for several globally rescaled resolutions in $1/p_t$.

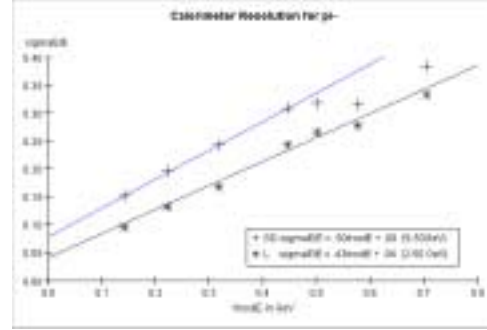


Figure 15.14: Expected π^- energy resolution in the L ($\sigma_E/E = 0.43/\sqrt{E} + 0.04$) and SD ($\sigma_E/E = 0.50/\sqrt{E} + 0.08$) Detectors.

of 200 cm. The electromagnetic energy resolution is expected to be $17\%/\sqrt{E}$.

The hadronic calorimeter is 120 layers of 8 mm lead layers with 2 mm scintillator sampling. The entire calorimeter comprises 6.6 interaction lengths. The transverse segmentation of the scintillator in the hadronic calorimeter is $19\text{ cm} \times 19\text{ cm}$. Figure 15.14 presents the expected π^- energy resolution.

The hope is that the large BR^2 of the L design will allow jet reconstruction using energy flow at a more modest cost than Si/W, overcoming the limited transverse segmentation possible with scintillator and the larger Moliere radius of lead. But, since the transverse segmentation of the EMCal is much larger than the Moliere radius, it is not clear whether energy flow can be effectively carried out for L. This is in contrast to the SD case, where the fine segmentation allows one to have some confidence that an efficient EF reconstruction can be carried out. This is clearly an area where additional work with full shower simulations is required.

Since shower reconstruction for an EF algorithm for the American detectors is still in its infancy, one can in the meantime use parameterizations of calorimeter performance using a fast simulation. One would expect that the performance from full reconstructions will eventually approach that of the fast simulation. Therefore, for the following performance plots we apply the energy flow technique, but assume a perfect charged-neutral separation in the calorimeters. The appropriate charged track resolutions and EMCal resolutions are then applied. This assumption is not unreasonable for SD, but for L it is probably too idealized. In any case, our method should indicate the asymptotic limit of performance.

To examine jet energy resolution, we used $e^+e^- \rightarrow q\bar{q}$ events without ISR or beamstrahlung, and demanded that exactly two jets be reconstructed. Hence, $E_{\text{jet}} = \sqrt{s}/2 = E_{\text{beam}}$. An example distribution of the reconstructed jet energy, for $\sqrt{s} = 100$ GeV is given in Fig. 15.15. Only events with $|\cos\theta_{\text{thrust}}| < 0.8$ are included. The tail of the distribution is due to QCD and jet-finding effects, whereas the resolution we are interested in here is given by the Gaussian distribution near E_{beam} , and we take the σ of this fit as the resolution. Figure 15.16 gives the resolution (the asymptotic limit of performance without accounting for non-Gaussian tails, as described above) as a function of E_{jet} . A fit to these data gives

$$\frac{\sigma_{E_{\text{jet}}}}{E_{\text{jet}}} = \frac{0.18}{\sqrt{E_{\text{jet}}}}. \quad (15.1)$$

One should not expect to actually achieve this idealized resolution with the L calorimeter.

Another important and general measurement of performance is the jet-jet mass resolution. To examine this, we examine the process $e^+e^- \rightarrow ZZ \rightarrow \text{hadrons}$. Exactly four final-state jets were required. To get a distribution with little background, we require that one 2-jet combination have mass near M_Z , then plot the mass of the other jet pair, M_{jj} . An example M_{jj} distribution is given in Fig. 15.17 for $\sqrt{s} = 350$ GeV. Again, we fit a Gaussian to the distribution near $E_Z = E_{\text{beam}}$ to extract a measure of the M_{jj} resolution. This resolution, $\sigma_{M_{jj}}/M_{jj}$, is plotted vs. $E_Z = \sqrt{s}/2 \approx E_{jj}$ in Fig. 15.18. A fit to the data of the form $(A/\sqrt{E_Z}) \oplus B$ gives

$$\frac{\sigma_{M_{jj}}}{M_{jj}} = \frac{0.64}{\sqrt{E_Z}}, \quad (15.2)$$

with negligible constant term. To the extent that the dijets from a Z are perfectly identified and that no color connection or jet merging effects occur, the sampling term constant here should approach that for the single jet energy resolution given in (15.1). The degradation of dijet mass resolution from this ideal limit requires more study.

The 3 T solenoidal coil is located outside the hadronic calorimeter to optimize calorimeter performance. The inner radius of the solenoidal coil is 370 cm.

The muon system consists of 24 layers of 5 cm iron plates, with 3 cm gaps for RPC detectors. Axial strips of 3 cm pitch measure the ϕ coordinate to 1 cm precision in all 24 gaps, and every sixth gap provides azimuthal strips for a measurement of the z coordinate to 1 cm precision. The barrel muon system begins at a radius of 420 cm. Figure 15.5 illustrates the expected performance for the L detector.

4.2 SD detector for the high energy IR

The strategy of the ‘Silicon Detector’ (SD) is based on the assumption that energy flow calorimetry will be important. While this has not yet been demonstrated in

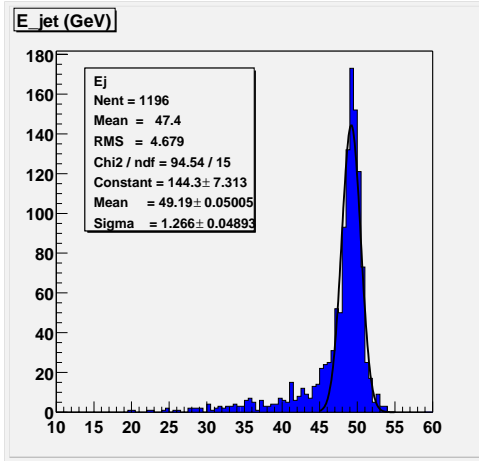


Figure 15.15: Reconstructed jet energy with the L detector for 50 GeV beam energy.

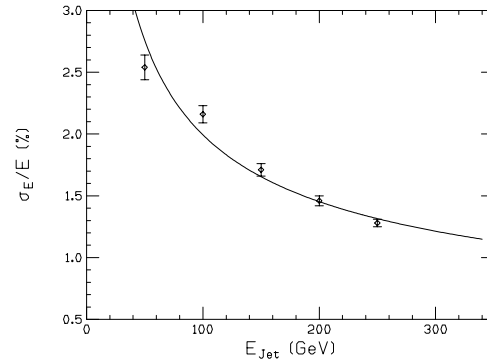


Figure 15.16: Jet energy resolution (in %) vs. jet energy for the L detector. The curve is the fit described in the text.

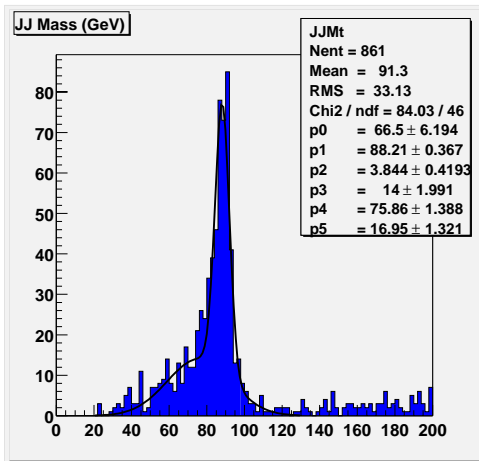


Figure 15.17: Reconstructed jet-jet mass for Z candidates in $e^+e^- \rightarrow ZZ \rightarrow$ hadrons at 350 GeV for the L detector.

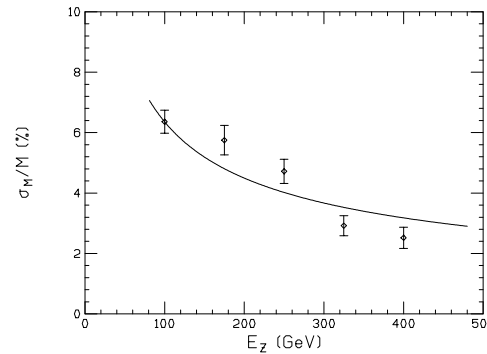


Figure 15.18: Jet-jet mass resolution (in %) for $Z \rightarrow 2$ jets vs. Z energy for the L detector in $e^+e^- \rightarrow ZZ \rightarrow$ hadrons events. The curve is the fit described in the text.

simulation by the American groups, the TESLA Collaboration has accepted it. This assumption then leads directly to a reasonably large value of BR^2 to provide charged-neutral separation in a jet, and to an electromagnetic calorimeter (EMCal) design with a small Moliere radius and small pixel size. Additionally, it is desirable to read out each layer of the EMCal to provide maximal information on shower development. This leads to the same nominal solution as TESLA: a series of layers of about 0.5

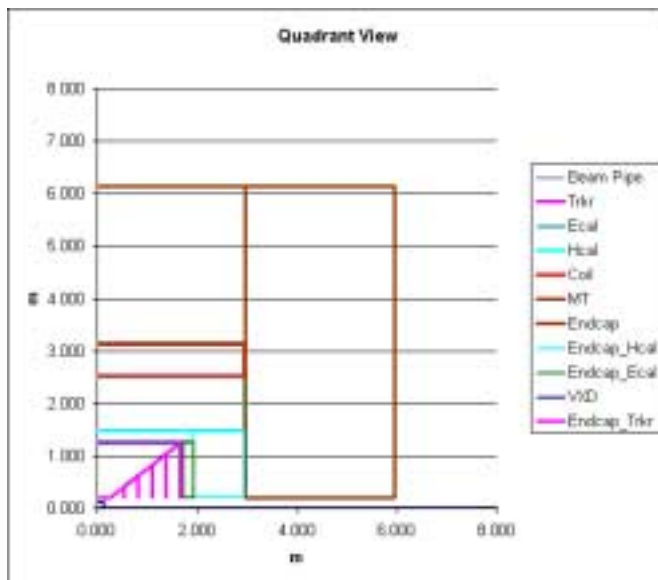


Figure 15.19: Quadrant view of the SD detector.

X_0 tungsten sheets alternating with silicon diodes. Such a calorimeter is expensive; its cost is moderated by keeping the scale of the inner detectors down. This has two implications: the space point resolution of the tracker should be excellent to meet momentum resolution requirements in a detector of modest radius, and the design should admit high-performance endcaps so that the barrel length (or $\cos \theta_{\text{Barrel}}$) will be small. Obviously it is desirable to minimize multiple scattering in the tracker, but compromises will be needed and must be tested with detailed simulation. The last real strategic question is whether the Hadronic Calorimeter (HCal) will be inside or outside the coil. Locating the HCal inside the coil permits reasonably hermetic calorimetry, but requires a larger, more expensive coil and more iron to return the flux. It is assumed that the detector will have an ultra-high-performance vertex detector based on CCD's or an equivalent thin, small pixel technology, as we have discussed for the L detector. A muon tracker will be interleaved in the iron flux return utilizing reliable RPC's or equivalent.

These considerations lead to a trial design with a tracking radius of 1.25 m and a field of 5 T. This is a BR^2 of 8, compared to 10 for TESLA and 12 for the L detector. The tracker is 5 layers of silicon strips with a $\cos \theta_{\text{Barrel}}$ of 0.8. Sets of five disks with silicon strips are arranged as endcaps to complete the acceptance. The HCal is inside the coil. The quadrant view is shown in Fig. 15.19, and the major dimensions are tabulated in Table 15.1.

The SD detector relies entirely upon silicon tracking in a 5 T solenoidal field in the central and forward regions. Its central and forward trackers consist of a 5-layer

silicon barrel—a silicon drift detector (SDD) or microstrips—and five layers of double-sided silicon microstrip forward disks. Figure 15.20 shows a sketch of the SD detector tracking system. The inner/outer radii of the barrel layers are 20/125 cm. The inner and outer disks are at 40 cm and 167 cm from the interaction point. The boundary between the barrel and disk system lies at $|\cos\theta| = 0.8$.

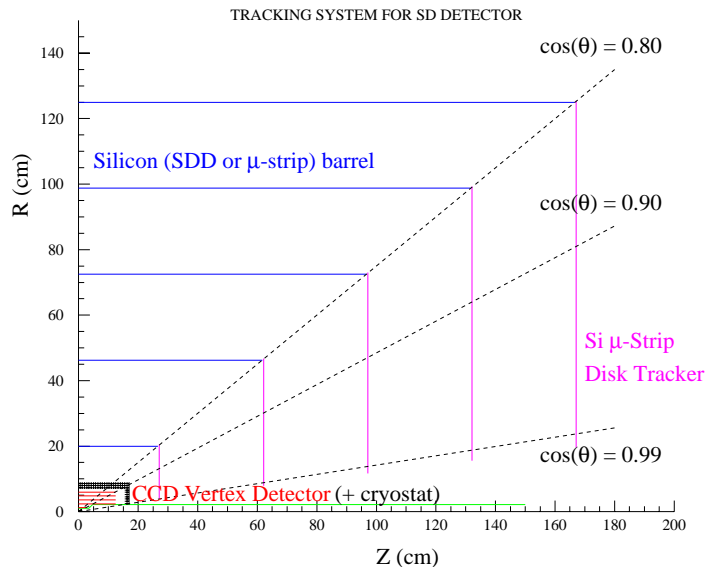


Figure 15.20: Sketch of SD detector tracking system.

The SDD option provides a solid-state analog to a time projection chamber. A potential gradient is applied via implanted cathodes in the silicon in order to force the generated electron cloud to drift through the bulk of the silicon to a collection anode. The highest voltage supplied to a single cathode can be up to 2500 V. By measuring the cloud distribution across the collection anodes and the drift time to the anodes in parallel, one records three-dimensional position information with a one-dimensional electronics readout. Three-dimensional position resolutions below $10\ \mu\text{m}$ in each dimension can be achieved with an anode spacing between 200 and $300\ \mu\text{m}$. Thus, the electronics cost is considerably reduced compared to other semiconductor detector options. Recently, a three-barrel SDD Tracker, using 216 large-area Silicon Drift wafers, was successfully completed and has been installed in the STAR experiment at RHIC.

Compared to the STAR detector the following modifications would be made to build a linear collider tracker: 1) increase the wafer size to $10\ \text{cm} \times 10\ \text{cm}$; 2) reduce the wafer thickness from 300 to $150\ \mu\text{m}$; and 3) redesign the front-end electronics for lower power to eliminate water cooling. The detector contains $56\ \text{m}^2$ of active silicon,

requiring about 6000 wafers and 4.4 million channels distributed over 229 ladders constructed from carbon-fiber material.

The silicon strip detector (SSD) option makes use of what is at this time a very mature tracking technology. Nevertheless, several avenues for further R&D are discussed below. It should be possible to exploit the small (order 10^{-5}) duty cycle of the linear collider to reduce the power dissipated by the readout electronics by switching to a quiescent state in between trains. This would substantially reduce the heat load, leading to a great reduction in the complexity and material burden of the mechanical structure.

In order to improve the robustness of the detector against linear collider backgrounds, it should be possible to develop a microstrip readout with a short shaping time, with timing resolution of order 5–10 nsec. This would allow out-of-time background hits to be eliminated from the bunch train with a rejection factor of better than 10:1.

On the other hand, the high granularity of microstrip detectors would make an SSD central tracker fairly robust against backgrounds even in the absence of intra-train timing. If instead it is felt that low- and intermediate-momentum track parameter resolution is more important than timing resolution, the use of a readout with a very long shaping-time should make it possible to implement detector ladders of substantially greater length than that of the 10–20 cm ladders of conventional strip detector systems. The AMS collaboration has developed a slow readout [19] with 6 electrons equivalent noise per cm of detector length. This may allow single ladders to stretch the entire half-length of the outermost silicon layer, and for the inner layers to be thinned. This, combined with a space frame that derives much of its support from the ladders themselves, would lead to a substantial reduction in the material burden, and give an overall low-momentum track parameter resolution on par with that of the L detector.

The forward disks for the SD tracker would have the same intrinsic performance as those described above for the L detector.

The performance of the SD detector tracking system, including the CCD vertex detector, is summarized in Fig. 15.11 and Fig. 15.12. In the limit of high-momentum tracks, the SD tracking resolution in $1/p_t$ is $2 \times 10^{-5} \text{ GeV}^{-1}$.

The EMCAL consists of layers of tungsten with gaps sufficient for arrays of silicon diode detectors mounted on G10 mother boards. The thickness of these gaps is a major issue, in that it drives the Moliere radius of the calorimeter. A thickness of 4 mm seems quite comfortable, accommodating a 0.3–0.5 mm silicon wafer, a 2 mm G10 carrier, and 1.5 mm of clearance. Conversely, 1.5 mm seems barely plausible, and probably implies a stacked assembly rather than insertion into a slot. For now, we assume a 2.5 mm gap.

It is expected that the readout electronics from preamplification through digitization and zero suppression can be integrated into the same wafer as the detectors. A

fallback would be to bump- or diffusion-bond a separate chip to the wafer. Thus it is expected that the pixel size on the wafer will not affect the cost directly. A pixel size between 5 and 10 mm on a side is expected. Shaping times would be optimized for the (small) capacitance of the depleted diode, but will probably be too long to provide any significant bunch localization within the train.

The HCal is chosen to lie inside the coil. This choice permits much better hermeticity for the HCal, and extends the solenoid to the endcap flux return. This makes a more uniform field for the track finding, and simplifies the coil design. The HCal absorber is a non-magnetic metal, probably copper or stainless steel. Lead is possible, but is mechanically more difficult. The detectors could be ‘digital’, with high-reliability RPC’s assumed. The HCal is assumed to be 4λ thick, with 34 layers of radiator 2 cm thick alternating with 1 cm gaps.

We have examined performance for the SD detector model in the same way as the L detector, calculating the asymptotic limit of performance. (See the corresponding discussion in Section 4.1 for the limitations of this analysis.) The electromagnetic energy resolution is expected to be $18\%/\sqrt{E}$. Figure 15.14 presents the expected π^- energy resolution. The resolution for jet energy reconstruction is given in Fig. 15.21. A fit to these data gives for the asymptotic limit

$$\frac{\sigma_{E_{\text{jet}}}}{E_{\text{jet}}} = \frac{0.15}{\sqrt{E_{\text{jet}}}} . \quad (15.3)$$

As previously, we fit a Gaussian to the distribution near $E_Z = E_{\text{beam}}$ to extract a measure of the M_{jj} resolution. This resolution, $\sigma_{M_{jj}}/M_{jj}$, is plotted vs. E_Z in Fig. 15.22. A fit to the data of the form $(A/\sqrt{E_Z}) \oplus B$ gives

$$\frac{\sigma_{M_{jj}}}{M_{jj}} = \frac{0.72}{\sqrt{E_Z}} , \quad (15.4)$$

with negligible constant term. These idealized studies are not yet precise enough to conclude that this is significantly worse than the L Detector performance.

The coil concept is based on the CMS design, with two layers of superconductor and stabilizer. The stored energy is 1.4 GJ, compared to about 2.4 GJ for the TESLA detector and 1.7 GJ for the L detector. The coil thickness is 60 cm, which is probably conservative.

The flux return and muon tracker is designed to return the flux from the solenoid, although the saturation field for the iron is assumed to be 1.8 T, which may be optimistic. The iron is laminated in 5 cm slabs with 1.5 cm gaps for detectors.

4.3 P detector for the lower-energy IR

The P Detector is proposed as a lower-cost detector for the second IR, capable of the performance required for lower-energy operation, including the Z -pole physics.

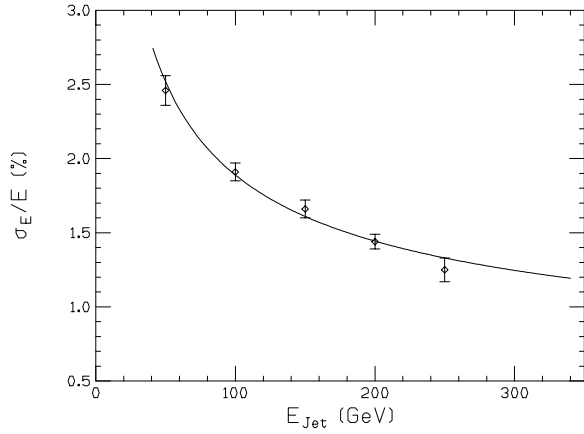


Figure 15.21: Jet energy resolution (in %) *vs.* jet energy for the SD detector. The curve is the fit described in the text.

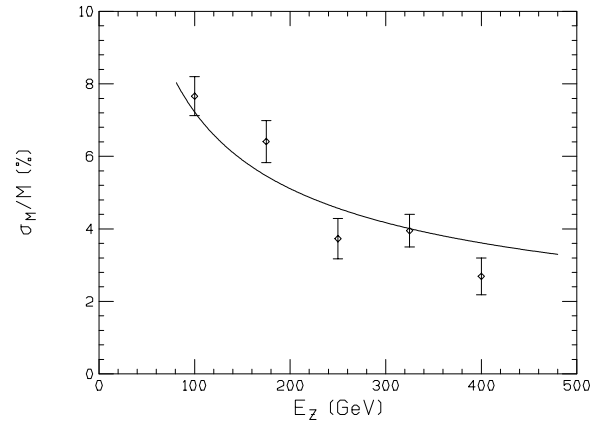


Figure 15.22: Jet-jet mass resolution (in %) for $Z \rightarrow 2$ jets *vs.* Z energy for the SD detector in $e^+e^- \rightarrow ZZ \rightarrow$ hadrons events. The curve is the fit described in the text.

The P detector is illustrated in Fig. 15.23. The dimensions of the P Detector are presented in Table 15.1.

The P detector employs the same CCD vertex detector design described for the L detector above, illustrated in Fig. 15.7.

The P detector's tracker design is modelled very closely upon that of the L detector. Since it is meant to operate at lower center-of-mass energies, its required resolution in $1/p_t$ is correspondingly less severe, allowing for a smaller tracking system and therefore a smaller, cheaper overall detector design. Figure 15.24 shows a sketch of the P detector tracking system.

Briefly, the P central tracker consists of a 120-layer TPC, of inner/outer radii = 25/150 cm and half-length 200 cm. Again, one or more intermediate tracking layers of silicon or scintillating fiber just inside the inner TPC radius may be desirable. The forward tracker consists of five silicon microstrip disks similar to those in the L and SD detectors. The performance of the P detector tracking system in a 3 T solenoidal field, including the CCD vertex detector, is summarized in Fig. 15.11 and Fig. 15.12. In the limit of high-momentum tracks, the P tracking resolution in $1/p_t$ is $6 \times 10^{-5} \text{ GeV}^{-1}$.

The 3 Telsa solenoidal coil is located outside the electromagnetic calorimeter and inside the hadronic calorimeter. This compromise (over the desire to move the coil outside the hadronic calorimeter) contains the cost of the P detector. The inner radius of the solenoid is 185 cm.

The electromagnetic calorimeter of the P Detector consists of 32 layers of lead-scintillator laminate, with 4 mm lead layers followed by 3 mm scintillator, for 22.8

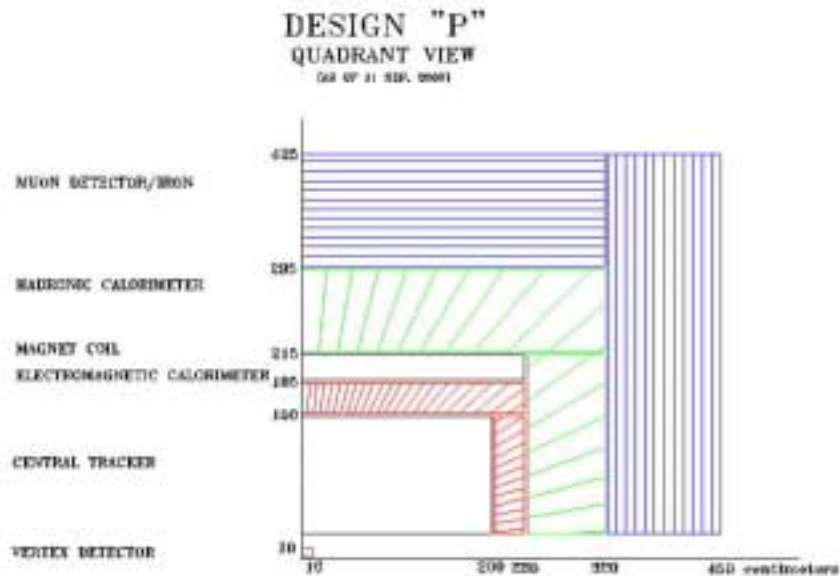


Figure 15.23: Quadrant view of the P detector.

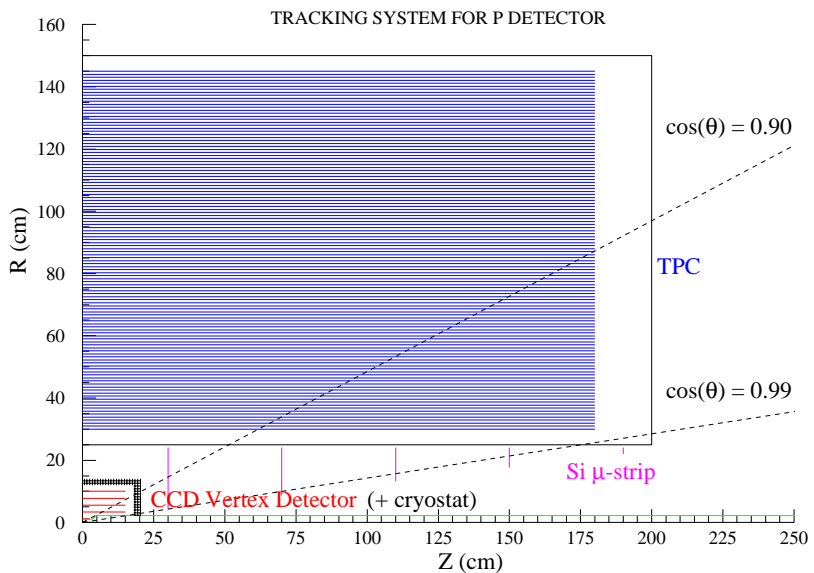


Figure 15.24: Sketch of P detector tracking system.

radiation lengths. These layers are ganged in pairs, giving 16 readout layers. One layer of 1 cm² silicon pads is foreseen near the EMCal shower maximum. The transverse segmentation of the scintillator is 2 degrees \times 2 degrees. It has an inner radius of 150 cm.

The hadronic calorimeter is 65 layers of 8 mm lead layers with 3 mm scintillator sampling. These layers are ganged to produce 8 independent samples. The inner radius of the hadronic calorimeter barrel is 215 cm. The entire calorimeter (electromagnetic and hadronic) comprises 3.9 interaction lengths. The transverse segmentation of the scintillator in the hadronic calorimeter is 4 degrees \times 4 degrees.

Given its segmentation, the P detector would not be well-suited for using energy flow in jet reconstruction. Unlike L and SD, the segmentation is organized as towers of constant θ and ϕ . For running at the Z , excellent jet reconstruction is probably not an important issue. However, at higher energy, for light Higgs or W -pair physics, for example, this conclusion is less clear. Jet reconstruction for P would most likely be carried out using the calorimeter alone (or the tracker alone). Note, however, that the Pb-scintillator ratio, as currently proposed, would not be expected to give good compensation of electromagnetic and hadronic energy depositions. Performance results for jet reconstruction, similar to those given for L and SD, have not yet been carried out. The results would provide an interesting point of comparison to the energy flow performance of SD.

The muon system consists of 10 layers of 10 cm iron plates, with 3 cm gaps for RPC detectors. Axial strips of 3 cm pitch measure the ϕ coordinate to 1 cm precision in all 10 gaps, and two gaps (5 and 10) provide azimuthal strips for a measurement of the z coordinate to 1 cm precision.

4.4 Cost estimates

The costs of the subsystems of each of the three detectors have been estimated based on past experience and escalation to FY01. The three cost estimates are shown in Table 15.2. Approximately 40% contingency is assumed for each of the detectors, resulting in a total cost estimate of \$359 million for the L detector, \$326 million for the SD detector, and \$210 million for the P detector.

References

- [1] TESLA Technical Design Report, http://tesla.desy.de/new__pages/TDR__CD/start.html
- [2] T. Matsui, in *Physics and Experiments with Future Linear Colliders (LCWS99)*, ed. E. Fernandez and A. Pacheco. (Univ. Auton. de Barcelona, Bellaterra, 2000).
- [3] C. Hensel, LC-DET-2000-001, Table 7 (2000).

Detector	L	SD	P
1.1 Vertex	4.0	4.0	4.0
1.2 Tracking	34.6	19.7	23.4
1.3 Calorimeter	48.9	60.2	40.7
1.3.1 EM	(28.9)	(50.9)	(23.8)
1.3.2 Had	(19.6)	(8.9)	(16.5)
1.3.3 Lum	(0.4)	(0.4)	(0.4)
1.4 Muon	16.0	16.0	8.8
1.5 DAQ	27.4	52.2	28.4
1.6 Magnet & support	110.8	75.6	30.5
1.7 Installation	7.3	7.4	6.8
1.8 Management	7.4	7.7	7.4
SUBTOTAL	256.4	242.8	150.0
1.9 Contingency	102.6	83.4	60.0
Total	359.0	326.2	210.0

Table 15.2: e^+e^- linear collider detector budgets (WBS to subsystem level) in M\$ FY01.

- [4] The SLD Collaboration, Nucl. Inst. and Meth. **A400**, 287 (1997).
- [5] J. E. Brau and N. Sinev, IEEE Trans. Nucl. Sci. **47**, 1898 (2000).
- [6] M. N. Frary and D. J. Miller, DESY 92-123A, Vol I, 1992, p. 379; D. Cinabro, in *Physics and Experiments with Future Linear Colliders*, ed. E. Fernandez and A. Pacheco. (Univ. Auton. de Barcelona, Bellaterra, 2000).
- [7] J.-C. Brient, in *Physics and Experiments with Future Linear e^+e^- Colliders (LCWS 2000)*, ed. A. Para. (AIP Conference Proceedings, 2001).
- [8] P. Gay, in *Physics and Experiments with Future Linear e^+e^- Colliders (LCWS 2000)*, ed. A. Para. (AIP Conference Proceedings, 2001).
- [9] P. Checchia, in *Physics and Experiments with Future Linear e^+e^- Colliders (LCWS 2000)*, ed. A. Para. (AIP Conference Proceedings, 2001).
- [10] T. Behnke, S. Bertolucci, R. Heuer, R. Settles, eds. DESY Pub: 2001-011 March 2001 Part III, A Detector for TESLA, p. IV-107.
- [11] A. Para, in *Physics and Experiments with Future Linear e^+e^- Colliders (LCWS 2000)*, ed. A. Para. (AIP Conference Proceedings, 2001).
- [12] R. J. Wilson, in *Physics and Experiments with Future Linear Colliders (LCWS99)*, ed. E. Fernandez and A. Pacheco. (Univ. Auton. de Barcelona, Bellaterra, 2000).
- [13] R. J. Wilson, in *Physics and Experiments with Future Linear e^+e^- Colliders (LCWS 2000)*, ed. A. Para. (AIP Conference Proceedings, 2001).

- [14] H. Yamamoto, in *Physics and Experiments with Future Linear Colliders (LCWS99)*, ed. E. Fernandez and A. Pacheco. (Univ. Auton. de Barcelona, Bellaterra, 2000).
- [15] M. Ronan and R. Settles, to appear in *Proceedings of the Vienna Instrumentation Conference*, Vienna, Austria, Feb 19–23, 2001.
- [16] R. Yarema *et al.*, Fermilab-TM-1892, June 1994 (revised Oct. 1996).
- [17] Boeing Electronic Systems, 3370 Miraloma Ave, Anaheim, CA 92803; M. D. Petroff *et al.*, *Appl. Phys. Lett.* **51**, 406 (1987).
- [18] For a cost breakdown, see
<http://www-mhp.physics.lsa.umich.edu/~keithr/LC/trackercosts.html>.
- [19] M. Fauluzzi, *Nucl. Inst. and Meth.* **383**, 35 (1996).